



Insights into the structure-property-activity relationship in molybdenum-doped octahedral molecular sieve manganese oxides for catalytic oxidation

Received 00th January 20xx,
Accepted 00th January 20xx

DOI: 10.1039/x0xx00000x

www.rsc.org/

Homer C. Genuino,^{a,b} Diego Valencia^c and Steven L. Suib^{a,d,e*}

Hexavalent molybdenum ions substituted into the mixed-valent framework of octahedral molecular sieve manganese oxides (1–10 mol% Mo-K-OMS-2) were systematically prepared *via* a single-step refluxing method. The structure, composition, morphology, thermal stability, and textural and redox properties of the Mo-K-OMS-2 materials were characterized by various experimental techniques. Density functional theory (DFT) calculations were performed to study the electronic properties of K-OMS-2 materials, including the influence of molybdenum on such properties. The catalytic activity of K-OMS-2 towards CO oxidation dramatically increased with Mo dopant concentration, until an optimum incorporation of 5 mol% was reached, giving full CO conversion at 120 °C (1 vol.% CO, 1 vol.% O₂). More importantly, the activity of the 5% Mo-K-OMS-2 catalyst was (reversibly) inhibited by water vapour (3%) in the feed only at low temperatures and exhibited better tolerance and stability during long-run experiments (28 h) as compared to undoped K-OMS-2. The superior performance of Mo-K-OMS-2 catalyst for CO oxidation can be attributed to the following factors: (1) Morphological evolution from nanofibers to nanospheres, as well as the slightly distorted structure, generated a sharp increase in the specific surface area up to 258 m² g⁻¹, hence, increased the number of surface active sites; (2) Improved mobility of reactive oxygen species at the surface and enhanced redox properties; and (3) Tailored electronic properties promoted more active sites for oxidation reactions, which is supported by DFT calculations.

Introduction

Octahedral molecular sieves (OMS) are a family of porous materials that naturally exist in the environment as manganese nodules in vast quantities on the sea floor.^[1–3] The synthetic counterpart, the cryptomelane-type manganese oxide or OMS-2, has a characteristic 2×2 tunnel structure as a result of the double chains of edge-sharing MnO₆ octahedra sharing corners with neighbouring chains.^[2–10] The presence of cations such as K⁺, NH₄⁺, or Na⁺ in the tunnel sites of OMS-2 is balanced by the reduction of some Mn⁴⁺ to Mn³⁺ and Mn²⁺ to stabilize the framework structure.^[2–10]

K-OMS-2 materials have been extensively studied for years for different applications including ion-exchange, chemical sensing, pollutant adsorptions, batteries, and many others.^[3–14] K-OMS-2 materials are excellent redox catalysts due to the mixed-valency of Mn atoms and their relevant adjustable physico-chemical properties. Such properties can be custom-designed using a number of strategies including the manipulation of synthetic process parameters such as temperature, pH, reaction time and pressure under hydrothermal conditions, and the use of different (co-)solvents. Introduction of metal cation(s) into the structure of K-OMS-2, in an effort to modify their redox properties and enhance their catalytic performance towards oxidation reactions, has also been undertaken. Doping by subtle introduction of an active metal into the tunnel or framework positions can improve their catalytic performance. Not only the activity, but also the selectivity of the K-OMS-2 catalyst is enhanced by introducing a single-type, low-valent metal cation (e.g., Ag⁺, Cu²⁺, Zn²⁺, or Co²⁺, Ni²⁺) in the tunnel sites or channels.^[15–21]

Doped K-OMS-2 materials are effective catalysts for total and preferential catalytic oxidation of CO. Indeed, catalytic CO oxidation is an important reaction for the treatment of effluent gas from industries and automobile exhausts, as well as the reforming gas in polymer electrolyte membrane fuel-cells.^[22–26] However, majority of the catalysts that are featured prominently for (low-temperature) CO oxidation are still those which contain relatively expensive noble metals. Nevertheless,

^a Department of Chemistry, University of Connecticut, 55 North Eagleville Road, Storrs, Connecticut, 06269-3060, United States.

^b Engineering and Technology Institute Groningen (ENTEG), Department of Chemical Engineering, University of Groningen, Nijenborgh 4, 9747 AG, Groningen, The Netherlands.

^c Dirección de Investigación en Transformación de Hidrocarburos, Instituto Mexicano del Petróleo, Eje Central Lázaro Cárdenas 152, Colonia San Bartolo Atepehuacán, C.P. 07730 Mexico City, Mexico

^d Institute of Materials Science, University of Connecticut, 97 North Eagleville Road, Storrs, Connecticut, 06269-3136, United States.

^e Department of Chemical and Biomolecular Engineering, University of Connecticut, 191 Auditorium Road, Storrs, Connecticut, 06269-3222, United States.

* Steven.Suib@uconn.edu; Tel.: +1-860-486-2797; Fax: +1-860-486-2981

† Footnotes relating to the title and/or authors should appear here.

Electronic Supplementary Information (ESI) available: [details of any supplementary information available should be included here]. See DOI: 10.1039/x0xx00000x

some cheaper alternatives such as those containing transition metals including metal oxides, spinels, perovskite, hopcalite, and alloys have been developed as potential catalysts.^[27-28] CO oxidation follows a redox mechanism over these catalysts. Lattice oxygen reacts with adsorbed CO and the gaseous oxygen from the feed replenishes oxygen vacancies that are otherwise formed by utilization of the former (i.e., Mars-van Krevelen mechanism).^[29-33]

More recent examples involving high-valent ion (i.e., pentavalent cations) incorporation in the K-OMS-2 framework were reported by some of us with the use of vanadium and niobium dopants.^[34-35] These studies provided some understanding of the effects of such dopants in the K-OMS-2 structure on the enhancement of catalytic activity and selectivity for CO oxidation. However, key understanding is still limited as to the dependency of catalyst performance towards CO oxidation on the interplay of catalyst composition modification (e.g., nature and concentration of a different cation), structure, and properties. A recent considerable interest is geared towards the generalization of the reflux synthetic approach by using other non-precious transition metal dopants.^[36-37] Despite this development, studies on the influence of, for example, hexavalent molybdenum dopant on catalytic performance are rather rare in the CO oxidation literature. Indeed, with the CO oxidation using manganese oxide catalysts being sufficiently established in the literature, insights into the structure and property changes in K-OMS-2 upon molybdenum doping and the associated activity enhancement therein will be imperative for better understanding of more intricate pore architectures belonging to the OMS family. Although limited gas-phase oxidation studies have been reported in the literature so far on the use of Mo-K-OMS-2 materials, they were previously used for chemical sensing applications and prepared using Na_2MoO_4 as a precursor synthesized *via* a conventional hydrothermal method.^[38] The abovementioned challenges form the basis for our choice to study Mo-doped K-OMS-2 materials for gas-phase catalytic oxidation.

In this present work, a surfactant-free, straightforward reflux method was used for substitutional doping of Mn by Mo at different concentrations into the K-OMS-2 framework. Doping K-OMS-2 allowed us to investigate this unique route to adjusting properties and hence catalytic efficiency enhancement of the parent material. This synthetic approach may be better than the deliberate application of physical deposition techniques, which often create secondary phases. A number of characterization techniques were employed to study the nature of Mo incorporation, elucidate the dominating factors for improved activity, and establish relationships between properties (i.e., structure, morphology, composition, surface area, porosity, thermal stability, reducibility) and performance. Application-relevant tests were performed to explore the effects of water vapour in the feed gas on the activity and intrinsic stability of the Mo-K-OMS-2 catalysts in long-term runs. The influence of such impurity on the reactivity of CO towards oxidation over this doped catalyst has not been demonstrated before. Reversible mode of catalyst inhibition

can be discerned that affects catalyst efficiency for CO oxidation. The results obtained can provide better understanding of catalyst stability against impurities and can guide rational catalyst design (e.g., by tuning surface properties). Finally, we demonstrate the beneficial effect of the Mo substitution on the catalytic performance of K-OMS-2 for CO oxidation based on electronic properties and density of states (DOS) obtained by density functional theory (DFT) calculations. Insights derived from this joint experimental and computational study on Mo-K-OMS-2 nanomaterials are reported for the first time.

Results and discussion

Characterization of the materials

The XRD patterns of the K-OMS-2 materials and commercial MoO_3 powder are shown in Figure 1. The undoped and Mo-K-OMS-2 materials show XRD patterns similar to a natural tetragonal structure of cryptomelane-type manganese oxide (JCPDS 29-1020). The absence of additional diffraction peaks attributed to Mo phases or any impurities in the doped K-OMS-2 materials suggest that a separate Mo compound did not form. The Mo^{6+} ions are instead highly dispersed into the unit cell of the K-OMS-2 structure. Samples with 1% and 2% Mo show the typical cryptomelane structure without any obvious impurities or additional phases, nor any shifts of peaks to higher 2θ , which

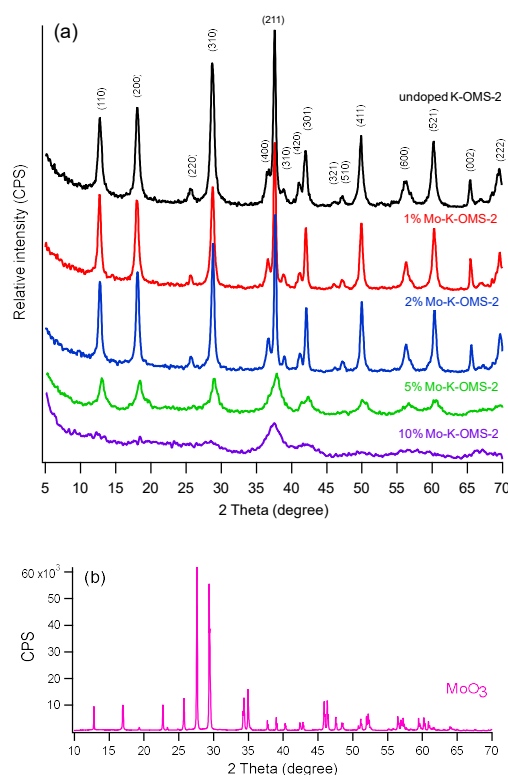


Figure 1. Powder XRD patterns of (a) undoped and Mo-doped K-OMS-2 materials and (b) commercial pure MoO_3 powder.

would correspond to smaller d spacings. Electronic and structural perturbations of K-OMS-2 structure are possible due to doping, however. Small decreases in peak intensities for Mo-K-OMS-2 especially at higher Mo loadings are observed. Reduction in peak intensity, as well as peak broadening, suggest that the doped K-OMS-2 materials have relatively low degree of crystallinity. For example, the XRD pattern of 5% Mo-K-OMS-2 shows considerable peak broadening due to the crystallite size effect or indicating the decrease of crystallite sizes (10 nm as determined by the Scherrer equation). The d -spacings (d_{110}) measured for undoped K-OMS-2 and 5% Mo-K-OMS-2 materials were 9.82 Å and 9.85 Å, respectively. The XRD pattern of K-OMS-2 containing 10% Mo-K-OMS-2 showed two broad peaks of very low intensity or almost no diffraction peaks, indicating this material is mostly amorphous/lacks long range order.

The Raman spectra of the undoped K-OMS-2 sample show characteristic spectra of K-OMS-2 materials with bands at ~ 580 and ~ 638 cm^{-1} (Figure 2). The weak band at ~ 580 cm^{-1} is due to Mn-O vibrations along the chains of the edge-sharing MnO_6 octahedra. The strong band at ~ 638 cm^{-1} is due to Mn-O lattice vibrations perpendicular to the MnO_6 octahedra. A significant change in intensity ratios in Mo-K-OMS-2 relative to undoped K-OMS-2 is observed. Furthermore, slight band shifts from ~ 638 cm^{-1} (more pronounced in the 5% Mo-K-OMS-2 and 10% Mo-K-OMS-2 materials) were observed. This small band shift can be attributed to the increment of the Mn-O-Mo bond vibrations provided by the Mo atoms during doping, which is in agreement with the XRD results. The Mo likely induced the decrease of particle size and variation of Mn valence, which could enhance mobility of lattice oxygen and expose more active sites for catalytic oxidation.^[36-37] The band at ~ 690 cm^{-1} in pure MoO_3 is ascribed to the Mo-O-Mo antisymmetric stretching vibration. The band at ~ 850 cm^{-1} can be attributed to Mo-O-Mo vibrations. All Raman spectra of doped K-OMS-2 samples lack strong bands (characteristic of Mo=O bond) in the regions of 310-370 cm^{-1} as well as 890-1000 cm^{-1} , indicating that Mo species are incorporated into the K-OMS-2 framework without the potential formation of separate MoO_x species and/or isolated particles.

The BET surface areas of the synthesized samples are summarized in Table 1. The surface areas of undoped, 1%, and 2% Mo-K-OMS-2 materials are comparable to the values reported for K-OMS-2 materials. The surface area of the 5% Mo-K-OMS-2 is significantly higher than those crystalline materials synthesized in this work. This result is one of the highest surface areas obtained so far for either 6+ valent single-species substituted K-OMS-2 materials grown by reflux methods. The amorphous 10% Mo-K-OMS-2 material has the highest surface area (258 m^2 g^{-1}) for these types of materials. The relatively higher BET surface areas of 5% and 10% Mo-K-OMS-2 materials indicate lowered degree of crystallinity and may be attributed to their unique morphologies. The pore volume of K-OMS-2 generally increased with increasing Mo doping. The average pore diameters of K-OMS-2 were within the range designated for mesoporous materials.

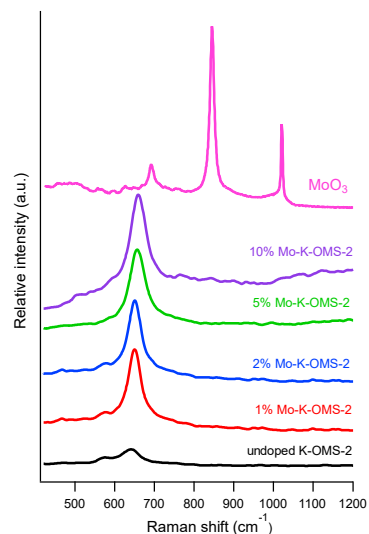


Figure 2. Raman spectra of undoped and Mo-doped K-OMS-2 materials, and commercial pure MoO_3 powder.

Table 1. Textural properties, elemental compositions, AOS of Mn, and hydrophobicity index of undoped and Mo-doped K-OMS-2 materials.

Material	Surface area (m^2 g^{-1}) ^a	Pore volume (cm^3 g^{-1}) ^b	Mole % Mo ^c (K:Mn)	AOS of Mn ^d	Hydrophobicity index
Undoped K-OMS-2	86	0.24	-	3.88	0.80
1% Mo-K-OMS-2	65	0.32	0.8 (1:8.3)	3.83	0.87
2% Mo-K-OMS-2	88	0.32	1.9 (1:8.3)	3.72	0.88
5% Mo-K-OMS-2	134	0.36	4.6 (1:8.7)	3.58	0.86
10% Mo-K-OMS-2	258	0.38	9.4 (1:9.5)	3.41	0.87

^a BET specific surface area determined by N_2 physisorption

^b BJH desorption cumulative pore volume determined by N_2 physisorption

^c Mole % Mo and K:Mn molar ratio determined by AAS

^d Average oxidation state of Mn determined by titrimetric methods

^e Hydrophobicity index determined by sorption experiments

The concentration of Mo as determined by atomic absorption spectroscopy (AAS) in doped materials are in good agreement with the expected concentrations calculated from the initial preparation mixtures. Moreover, the increasing concentration of Mo in the doped materials coincides with the reduction of the Mn concentration relative to K.

Mixed-valency is common in manganese oxide compounds and is a crucial property of redox catalysts. The average oxidation states (AOS) of Mn decrease with increasing Mo concentration and are indeed indicative of the mixed-valency of Mn, which is predominantly Mn^{4+} ions. The decreasing AOS of Mn furthermore indicates that the relative proportions of Mn^{3+} ions in 5% and 10% Mo-K-OMS-2 were significant. These low

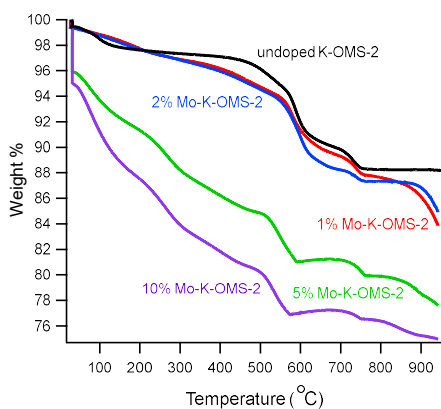


Figure 3. TGA profiles of undoped and Mo-doped K-OMS-2 materials.

AOS values can also be attributed to a high concentration of oxygen defects.^[39-40]

Variations in thermal stability can be correlated with changes in structure, morphology, or surface area of K-OMS-2 as a result of doping. The TGA profiles of 1% and 2% Mo-K-OMS-2 materials are similar with undoped K-OMS-2 in terms of shape of the curves and temperature regimes wherein major weight losses occur (Figure 3). However, a high overall weight loss at lower temperature regions is observed with 5% and 10% Mo-K-OMS-2 materials with high surface areas due to desorption of large amounts of physisorbed and chemisorbed H₂O and surface O₂ but without the loss of lattice oxygen, which could lead to structural collapse. The temperature of the second weight loss in doped K-OMS-2 is generally lower (~500 °C) as compared to 570 °C of the undoped K-OMS-2 sample, suggesting that there is a decrease in thermal stability after a certain level of Mo substitution.

The field-emission scanning electron microscopy (FESEM) and transmission electron microscopy (TEM) images of the K-OMS-2 materials reveal a systematic evolution in the morphology with increasing concentrations of Mo substitution (Figure 4). The undoped K-OMS-2 material shows a typical fibrous morphology, with periodic lattice planes being observed in the HRTEM images confirming excellent crystallinity in line with the XRD results. The crystalline 1% and 2% Mo-K-OMS-2 materials show different shapes with particles showing evidence of a morphological change from fibers to rod-like particles. The 5% Mo-K-OMS-2 sample, which has an even higher Mo concentration, reveals the presence of particles (10–15 nm) and suddenly the complete absence of elongated particles. The morphology of the 10% Mo-K-OMS-2 material is similar to that of 5% Mo-K-OMS-2, but significantly less crystalline. No molybdenum oxide particles were observed in all the samples, confirming structural homogeneity of the material. The morphology of the 5% and 10% Mo-K-OMS-2 materials is in fact reminiscent of a sponge with smaller particles forming the

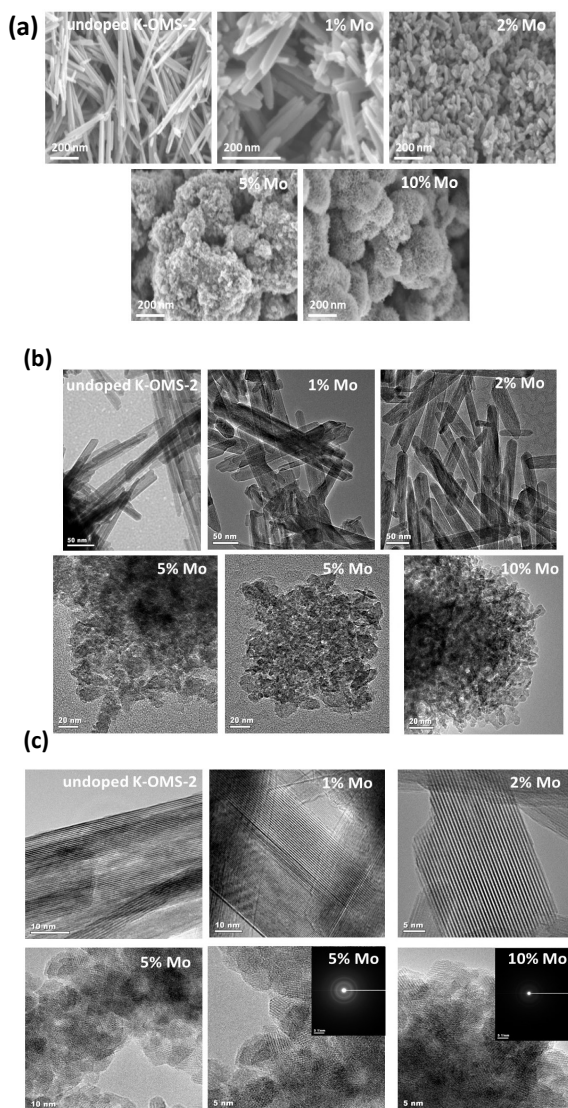


Figure 4. Representative (a) FESEM and (b-c) TEM images of undoped and Mo-doped K-OMS-2 materials.

nanosized crystallites. We can expect more exposed numbers of active sites on the edges of the particles in these sponge-like nanostructures, which play an important role in catalytic transformations.

Indeed, the length of the K-OMS-2 fibers significantly decreased as a function of Mo concentration. Insertion of molybdenum with higher oxidation state and mass than Mn⁴⁺ is thought to induce slight disorder in K-OMS-2, which is responsible for the reduction of the growth rate of fibers. The distortion of the ideal tetragonal crystal structure of cryptomelane lowers the symmetry to the monoclinic geometry when large cations substitute for mixed-valent Mn in the octahedral framework.^[36]

Catalytic testing of the materials

The catalytic performance of Mo-K-OMS-2 toward CO oxidation was then carried out (Figure 5). The 5% Mo-K-OMS-2 catalyst shows excellent activity and initiates the catalytic oxidation at a much lower temperature as compared to other catalysts. Undoped, 1%, and 2% Mo-K-OMS-2 show no observable catalytic CO conversion below 100 °C. The catalytic activity of the amorphous 10% Mo-K-OMS-2 catalyst was lower than the 5% Mo-K-OMS-2 catalyst, but better than the other concentrations, suggesting that Mo loading higher than 10% would have lower catalytic activity. In comparison, commercial MoO₃ was found to be completely inactive even up to 150 °C.

The activity of the most active catalyst (5% Mo-K-OMS-2) was maintained during continuous stability tests across a range of temperatures of different CO conversion results (Figure 5b). For example, the catalytic activity of 5% Mo-K-OMS-2 was maintained at ~60% and 100% at 150 °C under wet and dry conditions, respectively. This observation of stability is due to facile reversibility of oxygen re-adsorption (continuously replenished by O₂ in the feed gas) on Mo-K-OMS-2 surfaces. Oxygen species desorbed from Mo-K-OMS-2 can efficiently oxidize CO molecules without destruction of the cryptomelane structure giving good stability. Gaseous oxygen species can re-oxidize the reduced Mn species and maintained the activity of Mo-K-OMS-2 material during CO oxidation reaction. Expectedly, no significant changes in the crystal structure, textural properties, thermal stability, and redox properties of 5% Mo-K-OMS-2 were observed after stability runs at 150 °C under wet conditions (Figure S1).

The presence of water molecules blocks the active sites of K-OMS-2 catalysts thereby deactivating the material (Figure 5b-c). Catalyst poisoning was found to be more pronounced in CO oxidation reactions at near ambient temperatures. Remarkably, at moderate to high temperatures, the 5% Mo-K-OMS-2 showed better tolerance to water deactivation than undoped K-OMS-2 since there is enough energy for rapid desorption of water and for thermal activation of CO. Water poisoning is considered reversible or temporary. The hydrophobicity index of Mo-K-OMS-2 materials is higher than undoped K-OMS-2, hence the effect of moisture on activity is less (Table 1). Also recall that the catalytic activity can be attributed to the involvement of oxygen and these species (surface oxygen, hydroxyl groups, and oxygen vacancies due to Mo substitution) on the active sites are more pronounced in the 5% Mo-K-OMS-2 catalyst.

Having identified the 5% Mo-K-OMS-2 material as the best-performing catalyst, we focused our attention on investigating its redox properties using a temperature-programmed reduction (TPR) technique (CO as a reducing agent, Figure 6). The CO-TPR profiles show overlapped and dispersive desorption peaks in the range of ~175 to 425 °C. Typically, the reduction profile of MnO₂ comprises three distinct steps in order of increasing reduction temperature, which include the reduction of surface oxygen species, the reduction of MnO₂ to Mn₃O₄, and finally the transformation of Mn₃O₄ to MnO. The position and

shape of the peaks can be attributed to compositional difference between the two materials. Mo substitution at 5%

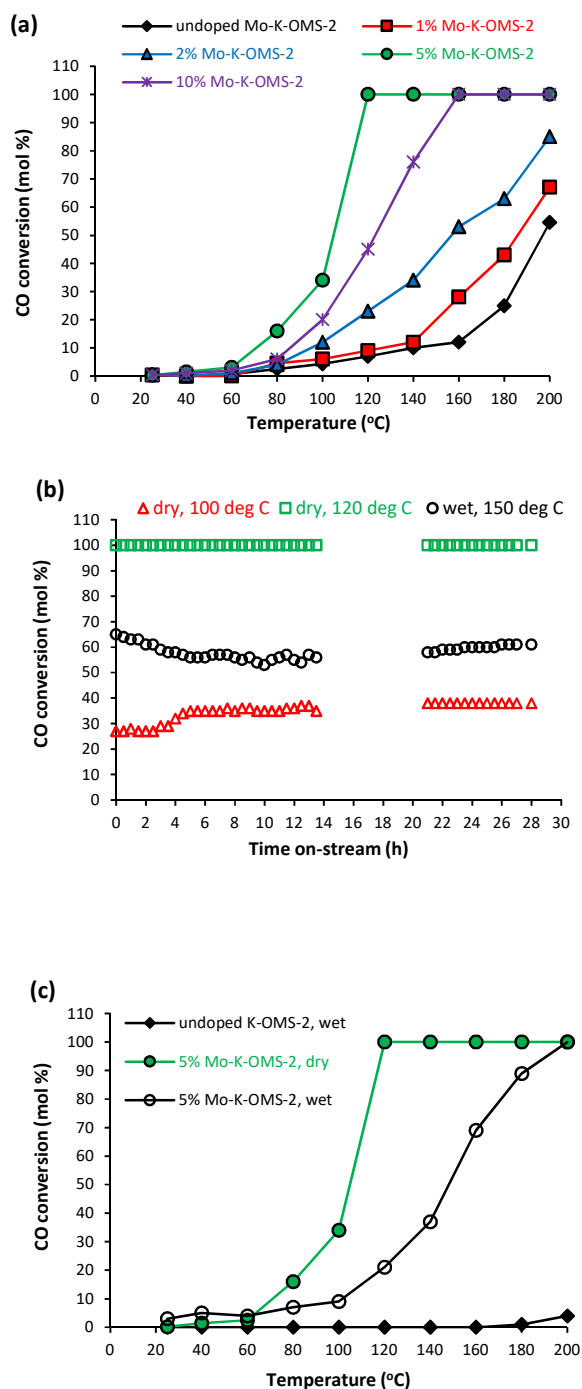


Figure 5. (a) Conversion as a function of temperature over undoped and Mo-doped K-OMS-2 catalysts, (b) Long-term stability of 5% Mo-K-OMS-2 catalyst under dry and moisture-rich conditions, and (c) Effects of water vapour on the activity of undoped and 5% Mo-K-OMS-2 catalysts. Conditions: 1% CO, 1% O₂, and 5% N₂ (internal standard) in He.

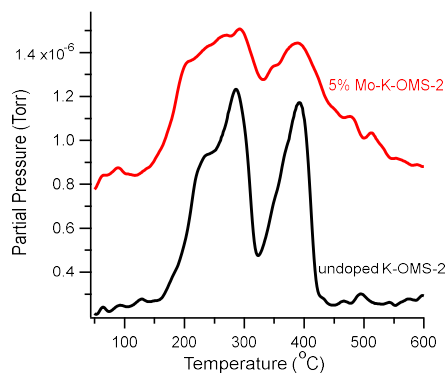


Figure 6. CO-TPR profiles of undoped and 5% Mo-K-OMS-2, the most active catalyst.

doping enhances the mobility and ease of removal of structural oxygen close to the surface of K-OMS-2, with a shift in reduction peaks to lower temperature regimes being evident, suggesting lower degree of crystallinity and enhanced Mn reduction, hence higher oxidation activity. Mo thus promoted the reduction of Mn ions. The involvement of lattice oxygen and the strong correlation between labile and lattice oxygen and catalytic activity suggest that the reaction proceed *via* the Mars-van Krevelen mechanism. No reduction bands attributed to Mo species were observed.

The oxidation state of Mo species in the as-prepared products was measured to be 6+ (Figure 7a). This is further elucidated from the difference in the binding energies of the Mo 3d_{5/2} peak at 231.8 eV and 3d_{3/2} at 234.9 eV and corresponding to the expectations based on the reduction potentials. The O 1s XPS spectra of 5% Mo-K-OMS-2 were deconvoluted into three elementary peaks attributed to three types of oxygen species on the surface (according to peak positions: the low BE peak due to lattice oxygen, the medium BE peak due to surface adsorbed oxygen, hydroxyl groups on the surface, and oxygen vacancies, and the high BE peak due to adsorbed molecular water). Compared to undoped K-OMS-2, 5% Mo-K-OMS-2 possessed poorer lattice oxygen species on the surface (O 1s XPS spectrum in Figure S2). Mo incorporation resulted in more surface cations in a low coordination environment, which could cause formation of surface defects including formation of oxygen vacancies. The low BE oxygen peak in 5% Mo-K-OMS-2 at 58% highlights that the fraction of catalytically active species are enriched near the surface to improve accessibility of reactant molecules. The resultant oxygen vacancies are thought to subsequently replenished by O₂ present in the feed stream during catalytic performance experiments.

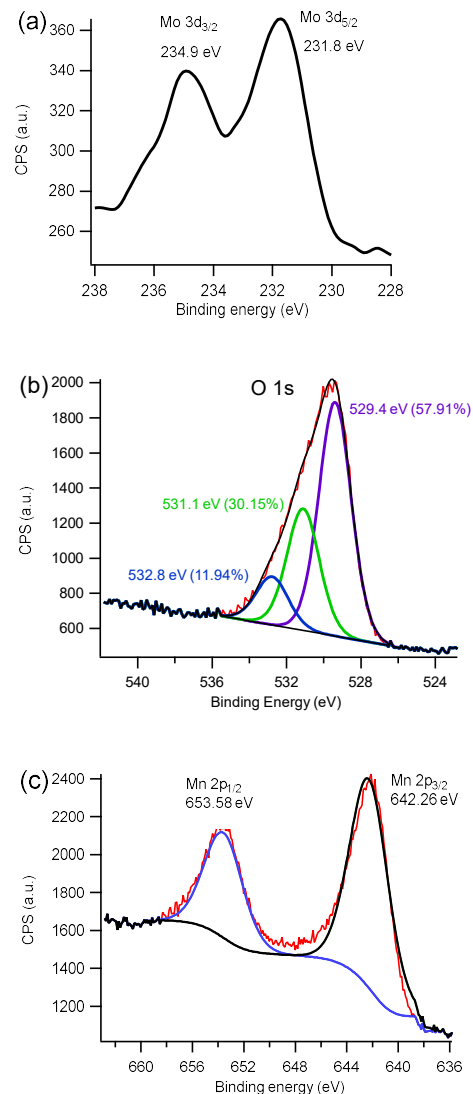


Figure 7. (a) Mo 3d, (b) O 1s, and (c) Mn 2p XPS spectra of the 5% Mo-K-OMS-2 material, the most active catalyst.

Computational studies

Selected optimized geometries of K-OMS-2 for the periodic calculations are illustrated in Figure 8. The isomorphous substitution of Mn by Mo within the structure is found to modify the lengths for the metal-oxygen bonds to a significant extent. The symmetry of the crystal structure had three different Mn-O bond lengths. These are also depicted for a comparison between undoped and Mo-doped material where the Mo had been structurally incorporated. The metal-oxygen bonds are larger for the Mo-K-OMS-2 as compared to K-OMS-2.

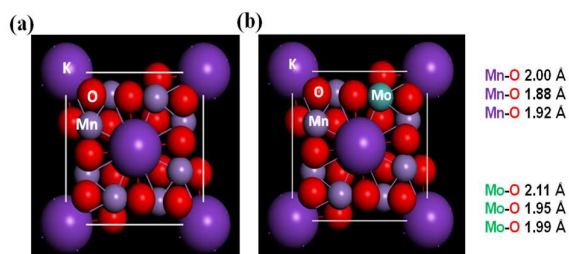


Figure 8. Optimized geometries for (a) undoped and (b) 5% Mo-K-OMS-2 materials. Selected and comparative bond lengths are summarized on the right side for both materials.

These results are in strong agreement with the morphological modifications that took place upon Mo doping due to these structural changes, which impact crystalline growth as well as stabilization of the structure of the materials. The larger Mo-O bond lengths compared to the Mn-O produce important changes in the crystalline structures resulting in a distorted structure. We obtained morphological evolution in the K-OMS-2 particles as shown in the TEM images that are related to this atomic perturbation within the molecular structures.

We next examined the electronic properties of the K-OMS-2 materials after selectively and incrementally substituting Mo in the mixed-valent octahedral framework. The density of states (DOS) for the different degree of substitution of Mn by Mo within the unit cell are shown in Figure 9. The substitution of Mo in the framework produces the modification in the DOS. The shape closer to the Fermi level is modified due to the subsequent substitution of Mn by Mo in the partial and total DOS. Mo is an element with higher electronegativity (2.16) than Mn (1.55). This difference allows Mo to pull electrons from Mn and lower the energy of the antibonding states.^[43] The incremental substitution of Mo in the parent material changes the gap between the bonding and antibonding orbitals. The contribution from the d orbitals to the DOS is remarkable at higher loadings of Mo into these materials. By changing the separation of the bonding and antibonding orbitals, Mo-K-OMS-2 materials showed a different behavior for redox processes, which make these materials more attractive for CO oxidation. The replacement of Mn atoms by Mo in the cryptomelane structure significantly improve the catalytic performance, reaching a maximum CO conversion for the 5% Mo-K-OMS-2 material. The modification of DOS is thus in good agreement with the catalytic activity due to the modification of the redox properties introduced into the cryptomelane structure by the Mo. That the experimental results showed morphological changes upon doping suggests experimental limitation of the substitution of Mn by Mo to maintain the parent cryptomelane structure. Related to this, we observed higher activity and enhanced CO conversion upon incorporation of Mo until 5 mol%.

The adsorption energy for CO molecule on the surface of K-OMS-2 at different contents of Mo is shown in Figure 10. The adsorption energy of CO on the parent material is calculated to

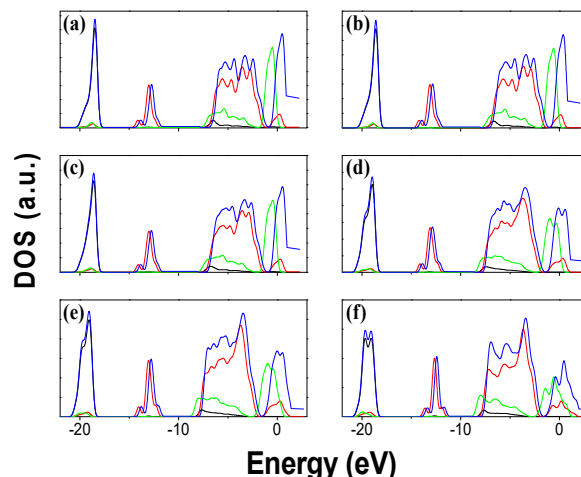


Figure 9. DOS for s (black), p (red), d (green), and total (blue). The % degrees of substitution of Mn by Mo in the K-OMS-2 unit cell are (a) 0, (b) 4, (c) 29, (d) 57, (e) 71, and (f) 100.

be $-49.9 \text{ kJ mol}^{-1}$. This adsorption energy is more exothermic than when Mo replaces Mn sites. The substitution of Mn by Mo resulted in a beneficial effect on the interaction of Mo with the CO. The higher value of the adsorption energy is located at about 7% of Mo, with a value of -77 kJ mol^{-1} . The CO interaction is expected to favour the catalyst substituted with Mo-K-OMS-2, for which we found the complete oxidation of CO at 100°C for the highly active catalytic material. The favourable adsorption of CO in this regime of the Mo loading is related to the electronic properties taking place by doping the material with a higher electronegative element in the cryptomelane structure.

Electronic properties indeed provide further insights into the effect of Mo substitution in the K-OMS-2 parent materials. We explained the morphological changes obtained experimentally

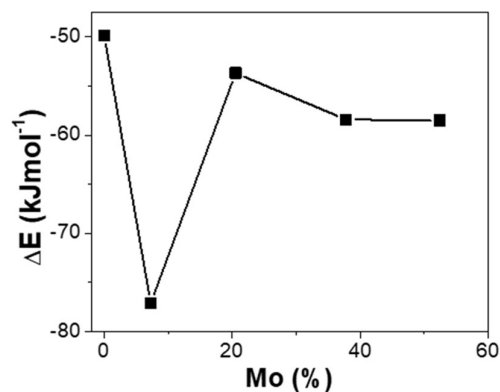


Figure 10. Calculated adsorption energies of CO on K-OMS-2 as a function of the Mo content.

with the larger metal-oxygen bonds due to Mo substitution in the materials framework. The band structure showed changes in the electronic changes and redox properties associated with Mo incorporation into the K-OMS-2 materials. The morphology of the particles described by textural studies and micrographs also have an impact on the catalytic performance. Nano-scale aggregates were found at 5% and 10% Mo-K-OMS-2 materials that showed more exposed or accessible sites on those catalysts and potentially more active Mo sites located on the surface materials. Characterization of these catalysts together with theoretical calculations thus give a better overview of the effects of Mo substitution at the bulk and atomic levels.

Overall, several factors explain the highly enhanced activity of the Mo-substituted K-OMS-2 materials. Low-doped Mo-K-OMS-2 materials (1-2% Mo) show similar catalytic behaviour, thus, the doping of Mo species does not impact the activities appreciably at lower Mo dopant concentrations. Differences in surface areas show a significant influence on the catalytic performance. Interestingly, catalytic activity is more likely to be dependent on the structures especially when one compares the catalytic results between the high surface area samples of 5% Mo-K-OMS-2 and 10% Mo-K-OMS-2. In addition, the characteristic mixed-valency systems are highly correlated with the preservation of structures with a noticeable difference of AOS values between these two samples, suggesting that mixed-valency is also important for activity improvement. All the results show that the 5% Mo-K-OMS-2 catalyst is at an optimum state of morphology, structure, and enhanced catalytic activity. Without detectable impurities or second phases by XRD, Raman spectroscopy, and HRTEM, the 5% Mo-K-OMS-2 material thus represents the approximate maximum Mo substitution of the K-OMS-2 structure.

The structural changes (particle size, morphology evolution, and electronic properties) are due to the compensation of structural instability caused by substitution, and indeed turn into an amorphous material beyond this point, such as shown by the properties of the 10% Mo-K-OMS-2 material. This observation is supported further by theoretical calculations. The best catalyst consisted of aggregates of nanosphere clusters from the physical packing of nano-sized fibrous particles, unique for K-OMS-2 materials. The fibrous nanoparticles would furnish a large number of adsorption sites. Aside from structural distortion leading to the morphological evolution, oxygen vacancies can enhanced catalytic activity in dry and moisture-rich conditions. Furthermore, the electronic structures show that modification of the bonding and antibonding gap can provide improved ability of the atoms to change their oxidation states under catalytic conversion of CO. Since the catalytic activity proved to be sensitive to the K-OMS-2 structures, the slightly distorted K-OMS-2 structure is correlated with the highly enhanced catalytic performance.

Conclusions

We have successfully synthesized Mo-doped K-OMS-2 materials as catalysts for CO oxidation *via* a straightforward reflux method. 5 mol% was found to be the concentration of Mo in the

K-OMS-2 material for a superior catalytic performance. The substitution of Mo produced important changes in structure, morphology, thermal behaviour, and electronic properties. Mo-K-OMS-2 materials produced nanospherical structures with high surface areas, which were unique when compared to the regular long fibrous morphology of undoped K-OMS-2. This observation was correlated with the significant reduction in crystallinity as the concentration of Mo was increased. We combined experimental characterization results with DFT calculations for a better understanding of the structure-property-activity relationship in the Mo-K-OMS-2 materials. Changes in the electronic properties allowed Mo-K-OMS-2 materials to enhance their performance towards CO oxidation reaction on the basis of DOS. Both complimentary results explained the changes in morphology as well as the more favourable interaction of CO with the Mo-K-OMS-2 catalysts. Lastly, we also demonstrated that Mo-K-OMS-2 as a more tolerant to and stable catalyst against water molecules poisoning than the undoped K-OMS-2 catalyst. These findings can help facilitate our understanding of the role of high-valent cation dopants in manganese oxides and the correlation of their structure and properties with enhanced performance in heterogeneous catalysis.

Acknowledgements

The authors acknowledge the support of the U.S. Department of Energy, Office of Basic Energy Sciences, Division of Chemical Sciences, Geosciences, and Biosciences for support of this research under contract DE-FG02-86ER13622. The authors also thank Dr. Heng Zhang and Dr. Lichun Zhang (University of Connecticut) for technical assistance and useful discussion.

Experimental and Computational Methods

Preparation of the catalysts

To synthesize undoped K-OMS-2 material, a solution containing 5.0 g of KMnO_4 in 100 mL of deionized water was prepared. A second solution was then prepared by dissolving 7.5 g of $\text{MnSO}_4 \cdot \text{H}_2\text{O}$ in 50.0 mL of deionized water and adding 8.5 mL of HNO_3 . This solution was subsequently added dropwise into the KMnO_4 solution with vigorous stirring forming a dark-brown precipitate. The resulting slurry was then refluxed overnight at 100 °C, washed with copious amount of deionized water, and dried overnight at 120 °C to obtain the K-OMS-2 material. To prepare 1%, 2%, 5%, and 10% Mo-doped K-OMS-2 materials, the preceding procedure was modified by adding appropriate amounts of the sodium molybdate (Na_2MoO_4) precursor into the KMnO_4 solutions. All chemicals were analytical grade and used without further purification. Commercial MoO_3 (99.97% trace basis) was used as received.

Experimental characterization of the materials

Powder X-ray diffraction (XRD) patterns were obtained using a Scintag 2000 XDS-2000 diffractometer equipped with Cu-K α

($\lambda=0.15406$ nm) radiation. The beam voltage and current used were 45 kV and 40 mA, respectively. Raman spectroscopy was performed at 514 nm with a Renishaw 2000 Raman microscope system, which included an optical microscope and a CCD camera for multichannel detection. Raman spectra of the samples were collected at 64 scans with a scan rate of 126 min^{-1} . Elemental analysis was conducted using a Perkin Elmer Model 3100 flame atomic absorption spectroscopy by standard addition methods. X-ray photoelectron spectroscopy (XPS) studies were done on a PHI model 590 spectrometer with microprobes using Al K α ($\lambda=1486.6$ eV) as radiation operated at an accelerating voltage of 12.5 kV. The powder samples were pressed onto carbon tapes mounted on double-sided adhesive copper tape stuck to a sample stage, where Mo 3d, Mn 2p, and O 1s transitions were recorded. Charging effects were corrected by adjusting the binding energy of C 1s to 284.6 eV.

The average oxidation state (AOS) of Mn in the K-OMS-2 materials was measured using a potentiometric titration method. The total manganese content was determined by digesting the samples and converting all of the manganese to Mn^{2+} and titrating to Mn^{3+} using standardized KMnO_4 . The AOS of manganese was then determined by reducing the manganese to Mn^{2+} with $(\text{NH}_3)_2\text{Fe}(\text{SO}_4)_2$ and back-titrating the excess Fe^{2+} with the KMnO_4 standard solution. Sorption of water by the materials was studied at room temperature by static weighing. Typically, a 200 mg sample of each material was heated at 250 °C for 4 h and placed in a desiccator containing saturated solutions of NH_4NO_3 or water. Uptake data were collected by accurately weighing the materials before and after overnight sorption. The surface areas of the synthesized materials were determined by the BET method using a Micrometrics ASAP 2010 instrument. The N_2 physisorption isotherms were obtained using a Quantachrome Autosorb-1-1C automated adsorption system at liquid nitrogen temperature. Prior to measurement, the samples were degassed at 120 °C overnight. The pore size distribution was determined by the BJH method and from the desorption isotherm.

The morphologies of the materials were recorded using a Zeiss DSM 982 Gemini FESEM with a Schottky emitter at an accelerating voltage of 2.0 kV and a beam current of 1.0 mA. The TEM images and elemental composition by EDXS were obtained using a JEOL JEM-2010 FaSTEM microscope equipped with an EDS detector operating at an accelerating voltage of 200 kV. The samples were dispersed in ethanol with ultrasonic treatment for at least 15 min, and drops of the suspension were placed on a copper grid for TEM studies. The thermal stability of the synthesized materials was determined using a Hi-Res TGA 2950 Thermogravimetric Analyzer in an ultrahigh pure N_2 atmosphere from 30–950 °C. TPR experiments were conducted using a gas mixture of 3% CO in He. Typically, a sample catalyst (0.2 g) was packed into a quartz tube supported by quartz wool and loaded into a programmable tube furnace. Prior to analysis, the sample was pretreated for 1 h by passing He gas (20 sccm) through the sample heated at 150 °C.

Catalytic Evaluation of the Materials for CO Oxidation

Typically, CO oxidation experiments were conducted in a quartz tubular fixed-bed flow-type reactor at atmospheric pressure with 100 mg of catalysts. The composition of feed gas was 1% CO, 1% O_2 , and 5% N_2 in He. The space velocity in all experiments was $12\,000 \text{ mL h}^{-1} \text{ g}_{\text{cat}}^{-1}$ and the reaction temperature range from 25 °C to 200 °C. Nitrogen was used as the internal standard for gas chromatography (GC) analysis. Prior to analysis, the sample catalyst was pre-treated for 1–2 h by passing He gas (20 sccm) through the sample heated at 150 °C. Application-relevant tests were analogously performed. Catalytic tests with moist feed gas (3% H_2O) were conducted by passing the feed gas through a water bubbler at room temperature. Helium was used as the carrier gas and the composition of the effluent gas was analysed online using an SRI model 8610C GC equipped with a 6' molecular sieve, a 6' silica gel column, and a thermal conductivity detector (GC-TCD). Peak areas were collected by allowing 30 min stabilization at each reaction temperature. The peak areas of CO, O_2 , N_2 , and CO_2 were proportional to their concentrations and were used for quantitative analysis. The formulas used to calculate the % CO conversion were:

$$(\text{Peak area CO})_{\text{initial}} = (\text{Peak area CO})_{\text{blank}} \times (\text{Peak area N}_2)_{\text{sample}} / (\text{Peak area N}_2)_{\text{blank}}$$

$$\text{CO Conversion} = (\text{Peak area CO})_{\text{initial}} - (\text{Peak area CO})_{\text{sample}} / (\text{Peak area CO})_{\text{initial}} \times 100\%$$

Computational Details

A model was constructed based on our previous work reporting the crystallographic data of K-OMS-2.^[18] K-OMS-2 consists of double-wide slabs of edge-shared MnO_6^{8-} octahedra. The tunnels are bound by four $\text{Mn}_2\text{O}_6^{4-}$ slabs, each rotated 90° to its neighbor, and joined through corner-shared O atoms. The unit cell (I4/m space) contains 16 O atoms and 8 Mn sites. The surface model was represented with a 3D periodic slab model. The periodic cell contains three units per cell of truncated K-OMS-2 with periodic boundary conditions. Geometry optimization and electronic properties were carried out using the revised version of the PBE^[44] functional that has shown excellent performance for chemisorption in catalysis^[45], using double numerical with polarization (DNP) basis sets. The threshold of density matrix convergence was set to 10^{-5} . A Fermi smearing of 0.05 Hartree and a real-space cut-off of 4.9 Å were also used to get the computational convergence for this system. Adsorption energies were obtained at the same level of theory by creating a small cluster to interact with CO molecules. All the calculations were performed using the DMol³ software.

Notes and references

- 1 Y. F. Shen, R. P. Zerger, R. N. De Guzman, S. L. Suib, L. Mc Curdy, D. I. Potter, C. L. O'Young, *Science*, 1993, **260**, 511–515.
- 2 S. L. Suib, *Acc. Chem. Res.*, 2008, **41**, 479–487.

- 3 H. Genuino, H. Huang, E. Njagi, L. Stafford, S.L. Suib, A Review of Green Synthesis of Nanophase Inorganic Materials for Green Chemistry Applications. In *Handbook of Green Chemistry*, Part 8: Green Nanoscience. 2012, 217-244.
- 4 Z.-R. Tian, W. Tong, J.-Y. Wang, N.-G. Duan, V. Krishnan, S. L. Suib, *Science*, 1997, **276**, 926-930.
- 5 S. L. Brock, N. Duan, Z. R. Tian, O. Giraldo, H. Zhou, S. L. Suib, *Chem. Mater.*, 1998, **10**, 2619-2628.
- 6 Y.-C. Son, V. D. Makwana, A. R. Howell, S. L. Suib, *Angew. Chem. Int. Ed.*, 2001, **40**, 4280-4283.
- 7 X. Chen, Y.-F. Shen, S. L. Suib, C. L. O'Young, *Chem. Mater.*, 2002, **14**, 940-948.
- 8 S. Gomez, L. J. Garces, J. Villegas, R. Ghosh, O. Giraldo, S. L. Suib, *J. Catal.*, 2005, **233**, 60-67.
- 9 S. L. Suib, *J. Mater. Chem.*, 2008, **18**, 1623-1631.
- 10 H. Huang, C.-H. Chen, L. Xu, H. Genuino, J. Garcia-Martinez, H.F. Garces, L. Jin, , C. King'ondeu, S. L. Suib, *Chem. Comm.*, 2010, **46**, 5945-5947.
- 11 M. Huang, F. Li, F. Dong, Y. X. Zhang, L. L. Zhang, *J. Mater. Chem. A.*, 2015, **3**, 21380-21423.
- 12 T. Oishi, K. Yamaguchi, N. Mizuno, *ACS Catal.*, 2011, **1**, 1351-1354.
- 13 M. Hua, S. Zhang, B. Pan, W. Zhang, L. Lv, Q. Zhang, *J. Hazard. Mater.*, 2012, **211-212**, 317-331.
- 14 S. Luo, L. Duan, B. Sun, M. Wei, X. Li, A. Xua, *Appl. Catal. B.*, 2015, **164**, 92-99.
- 15 G. G. Xia, Y. G. Yin, W. S. Willis, S. L. Suib, *J. Catal.*, 1999, **185**, 91-105.
- 16 L. Li, D. L. King, *Chem. Mater.*, 2005, **17**, 4335-4343.
- 17 J. Chen, X. Tang, J. Liu, E. Zhan, J. Li, X. Huang, W. Shen, *Chem. Mater.*, 2007, **19**, 4292-4299.
- 18 C. Calvert, R. Joesten, K. Ngala, J. Villegas, A. Morey, X. Shen, S.L. Suib, *Chem. Mater.*, 2008, **20**, 6382-6388.
- 19 R. Hu, L. Xie, S. Ding, J. Hou, Y. Cheng, D. Wang, *Catal. Today*, 2008, **131**, 513-519.
- 20 H. C. Genuino, S. Dharmarathna, E.C. Njagi, M.C. Mei, S.L. Suib, *J. Phys. Chem. C.*, 2012, **116**, 12066-12078.
- 21 M. Ozacar, A. S. Poyraz, H. C. Genuino, C. H. Kuo, Y. Meng, S. L. Suib, *Appl. Catal. A.*, 2013, **462-463**, 64-74.
- 22 A. V. Salker, R. K. Kunkalekar, *Catal. Commun.*, 2009, **10**, 1776-1780.
- 23 Y. M. Dai, T. C. Pan, W. J. Liu, J. M. Jehng, *Appl. Catal. B.*, 2011, **103**, 221-225.
- 24 Z. Qu, W. Huang, M. Cheng, X. Bao, *J. Phys. Chem. B.*, 2005, **109**, 15842-15848.
- 25 R. Xu, X. Wang, D. Wang, K. Zhou, Y. Li, *J. Catal.*, 2006, **237**, 426-430.
- 26 R. Hu, C. Yan, L. Xie, Y. Cheng, D. Wang, *Int. J. Hydrogen Energy*, 2011, **36**, 64-71.
- 27 R. Song, S. K. Kang, S. D. Kim, *Catal. Lett.*, 1997, **49**, 65-68.
- 28 R. Prasad, P. Singh, *Catal. Rev. Sci. Eng.*, 2012, **54**, 224-279.
- 29 R. Hu, Y. Cheng, L. Xie, D. Wang, *Chin. J. Catal.*, 2007, **28**, 463-468.
- 30 L. Lamatia, M. A. Peluso, J. E. Sambeth, H. Thomas, G. Mineli, P. Porta, *Catal. Today*, 2005, **107-108**, 133-138.
- 31 J. Luo, Q. Zhang, J. Garcia-Martinez, S. L. Suib, *J. Am. Chem. Soc.*, 2008, **130**, 3198-3207.
- 32 V. D. Makwana, Y.-C. Son, A. Howell, S. L. Suib, *J. Catal.*, 2002, **210**, 46-52.
- 33 V. P. Santos, M. F. R. Pereira, J. J. M. Órfão, J. L. Figueiredo, *Appl. Catal. B.*, 2007, **72**, 129-135.
- 34 H. C. Genuino, Y. Meng, D. T. Horvath, C.-H. Kuo, A. M. Morey, R. Joesten, S. L. Suib, *ChemCatChem*, 2013, **5**, 2306-2317.
- 35 H. C. Genuino, M. Seraji, Y. Meng, D. Valencia, S. L. Suib, *Appl. Catal. B.*, 2015, **163**, 361-369.
- 36 C. Chen, E. C. Njagi, S. Y. Chen, D. T. Horvath, L. Xu, A. Morey, C. Mackin, R. Joesten, S. L. Suib, *Inorg. Chem.* (54) 2015, 10163-10171.
- 37 T. Uematsu, Y. Miyamoto, Y. Ogasawara, K. Suzuki, K. Yamaguchi, N. Mizuno, *Catal. Sci. Technol.*, 2016, **6**, 222-233.
- 38 M. Polverejan, J.C. Villegas, S. L. Suib, *J. Am. Chem. Soc.* 2004, **126**, 7777-7775.
- 39 R. Wang, J. Li, *Environ. Sci. Technol.*, 2010, **44**, 4282-4287.
- 40 F. Cheng, J. Shen, B. Peng, Y. Pan, Z. Tao, J. Chen, *Nat. Chem.* 2011, **3**, 79-84.
- 41 T. Gao, P. Norby, *Eur. J. Inorg. Chem.*, 2013, **2013**, 4948-4957.
- 42 Y. Yuan, S. M. Wood, K. He, W. Yao, D. Tompsett, J. Lu, A. Nie, M. S. Islam, R. Shahbazian-Yassar, 2016, **10**, 539-548.
- 43 D. A. Kuznetsov, B. Han, Y. Yu, R. R. Rao, J. Hwang, Y. Román-Leshkov, Y. Shao-Horn, *Joule*, 2018, **2**, 225-244.
- 44 Y. Zhang, W. Yang, *Phys. Rev. Lett.*, 1998, **80**, 890.
- 45 B. Hammer, L. B. Hansen, and J. K. Nørskov, *Phys. Rev. B.* 1999, **59**, 7413-7421.